Three-Dimensional Finite Element Modelling of Chemical Environment in Droplet-based Microfluidic Systems for Drug Therapy Applications

Zsombor Szomor,[1,2,a)] Nafisat Gyimah,[3,b)] Tamás Pardy,[3,4,c)] and Péter Fürjes[1,d)]
[1)] *Microsystems Lab., Inst. of Technical Physics and Materials Science, HUN-REN Centre for Energy Research, Budapest, Hungary*
[2)] *Doctoral School on Materials Sciences and Technologies, Óbuda University, Budapest, Hungary*
[3)] *Thomas Johann Seebeck Department of Electronics, Tallinn University of Technology, Tallinn, Estonia*
[4)] *Department of Electron Devices, Budapest University of Technology and Economics, Budapest, Hungary*

(Dated: 12 June 2025)

This study presents a novel Computational Fluid Dynamics (CFD)-based optimization framework for enhancing mixing efficiency in droplet-based microfluidic systems. The key innovation lies in systematically linking microchannel geometry, flow parameters, and material properties to internal mixing dynamics—providing new insights into how microfluidic design can be tuned for improved solute distribution within droplets. Such optimization is particularly relevant for applications in single-cell analysis and on-chip therapeutic drug screening. Using water and solution of fluorescently dyed Bovine Serum Albumin (BSA) as the dispersed phase within a silicone oil-based continuous phase, we generated quasi-monodisperse droplets and analyzed how mixing behavior responds to specific design choices. Simulations revealed that serpentine channels enhanced mixing efficiency by up to 17% compared to straight channels, primarily due to Dean vortices that promote homogenization. Flow rate manipulation further influenced droplet formation and internal mixing: initial flow conditions (0.2 μl/s water, 0.2 μl/s BSA, 0.02 μl/s oil) resulted in stable but poorly mixed droplets, while increasing the oil flow rate to 1.4 μl/s triggered a droplet-generation regime that significantly improved internal mixing. Experimental measurements of droplet behavior and internal intensity profiles were conducted to validate the simulation results, showing strong qualitative agreement and confirming the predictive capability of the proposed model. These findings highlight the potential of droplet microfluidics as a platform for miniaturized chemical reactors, enabling precise control over solute concentration and distribution. This approach provides a foundation for precise drug delivery for studying therapeutic agents and supports the development of advanced lab-on-a-chip systems for optimized drug formulation within controlled microenvironments.

Keywords: multi-phase microfluidics, finite element modelling (FEM), droplet generation, mixing

I. INTRODUCTION

The development and application of compact models of tissues or cell populations support the understanding of physiological processes and disease mechanisms at the cellular level while accelerating pharmaceutical drug development experiments. These cell-scale models can be established using microfluidic systems designed to manipulate the chemical environment of individual cells or cell populations within microreactors[1,2]. Specific three-phase microfluidic systems have been developed to generate stable suspensions of droplets, forming closed chemical environments around single cells. Over the past two decades, the integration of micro-engineered systems has transformed the landscape of chemical and biological sciences, particularly in high-throughput analyses. The fabrication of sophisticated microfluidic architectures has enabled researchers to devise innovative experimental platforms for efficiently processing small analytical volumes[3]. Droplet-based microfluidic systems operate by partitioning the sample or reagent phase into discrete, physically isolated droplets using an immiscible carrier phase, leading to significant changes in fluid dynamics. However, achieving efficient mixing within such systems poses a major challenge due to the dominance of laminar flow, which inherently limits mixing efficiency[4]. Passive microfluidic techniques address this challenge effectively by leveraging channel geometries with intricate patterns, such as serpentine or spiral designs, to induce chaotic advection and vortices, thereby enhancing mixing performance without external energy sources[5,6].

Mixing reagents with the test solution is critical for reliable results in most immunoassays and cellular or molecular determination methods. This becomes even more significant in miniaturized systems, where mixing efficiency is constrained by laminar flow. A crucial aspect of in vitro cell analysis involves isolating cells in microfluidic environments to observe their behavior under

[a)] Electronic mail: szomor.zsombor@ek.hun-ren.hu; Corresponding author. ORCID: 0009-0004-2262-548X
[b)] Electronic mail: nafisat.gyimah@taltech.ee
[c)] Electronic mail: tamas.pardy@taltech.ee
[d)] Electronic mail: furjes.peter@ek.hun-ren.hu; ORCID: 0000-0002-8022-4367

controlled conditions. Finite Element Modeling (FEM)[7] was employed in this study to explore the influence of microfluidic channel geometry on mixing efficiency, fluid dynamics, and concentration transport phenomena in three-phase droplet-based systems. Unlike previous studies that primarily focused on two-phase systems, this work incorporates a three-phase model (water, fluorescent BSA solution, oil) to simulate real-world applications more accurately, particularly in pharmaceutical and diagnostic research. The investigation examined Dean's vortices, which enhance mixing by creating lateral liquid movement in curved channels, and their effects on the transport of Bovine Serum Albumin (BSA) solutions[8] mixed with water within droplets suspended in an oil carrier phase.

This research enhances microfluidic mixing studies by utilizing fluorescence-based concentration monitoring, allowing for precise real-time visualization of molecular distribution within droplets—essential for drug delivery applications requiring homogeneous therapeutic dispersion. In contrast to previous works[5,6,9,10] that primarily assess mixing through indices, this method offers deeper biomolecular insights and enables the potential substitution of BSA with fluorescent therapeutic agents like doxorubicin. By adopting a three-phase model, this study provides a more accurate representation of real-world scenarios, particularly in pharmaceutical and diagnostic applications, by capturing droplet behavior and molecular transport more effectively[11]. The findings are especially significant for immunoassays and cell studies, where droplets function as controlled microenvironments for biochemical reactions. By integrating a comprehensive three-phase approach, fluorescence-based tracking, pharmaceutical relevance, and thorough validation techniques, this study supports the development of more advanced and efficient microfluidic platforms.

II. MATERIALS AND METHODS

A. Definition of the hydrodynamic model

One of the primary attributes of the microfluidic environment is the prevalence of surface viscous forces, which exert significant influence due to the small dimensions. Consequently, a predominantly laminar flow pattern emerges, characterized by the non-intersecting coflow of liquid layers.

For the characterization of microfluidic systems, the Capillary number (Ca) serves as a commonly utilized parameter[12]. By leveraging the Capillary number, the interplay among surface tensions, channel geometry, and viscous forces can be effectively assessed, facilitating the description of a three-phase microfluidic system and its variations. Moreover, in the context of three-phase flow systems, the Capillary number enables the characterization of the impact of hydrodynamic parameters on droplet formation. The Capillary number can be expressed as follows:

$$Ca = \frac{\mu_c a \Delta U}{\gamma \Delta z} = \frac{\mu_c Q_c a}{\sigma h \Delta z}\left(\frac{1}{w_{or}} - \frac{1}{2w_c}\right) \quad (1)$$

where μ_c is the viscosity of the continuous phase, a is half of the channel width of the dispersed phase, σ is the interfacial tension between the two phases (also known as γ), $\Delta U/\Delta z$ is the effective rate of strain (also known as G), Q_c is the volume flow of the continuous phase, h is the depth of the channel, Δz is the distance between the channel of the dispersed phase and the outlet of the orifice, ω_{or} is the cross-sectional width of the orifice structure, and ω_c is the width of the inlet channel of the continuous phase. The utilized geometry for the simulations adheres to the overarching structure and parameters outlined in Figure 1.

By adjusting the Capillary number following alterations in geometry and flow rates, it becomes feasible to regulate droplet sizes conveniently, thereby attaining the desired dimensions for their utilization as microreactors.

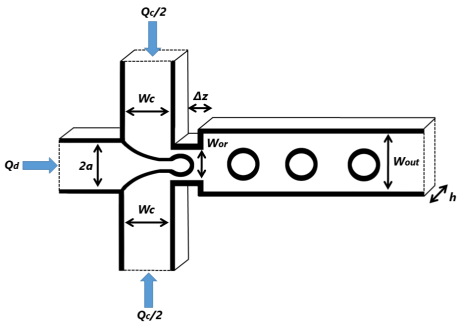

FIG. 1. Geometric parameters for calculating the Capillary number (1) in droplet formation microfluidic architecture

The values of the geometric parameters influencing the Capillary number can be seen in Table I. The main droplet generation region remained the same regarding the two geometries. After that, the channel length and shape changed to achieve different mixing properties.

TABLE I. Geometric parameters of the model.

W_c	W_{or}	W_{out}	a	Δz	h
200 μm	50 μm	200 μm	100 μm	25 μm	50 μm

In addition to the Capillary number, channel confinement plays a crucial role in droplet formation and deformation[13,14]. When droplets are strongly confined by the channel walls, they experience pronounced elongation and increased deformation due to geometric constraints. This confinement alters the local flow field and

redistributes viscous stresses, which subsequently influences the critical Capillary number for droplet breakup as well as the droplet generation regime. As the confinement ratio—the ratio of droplet diameter to channel height—approaches unity, droplets tend to elongate further along the flow direction and exhibit delayed pinch-off, consistent with a squeezing breakup mechanism rather than unconfined dripping. By carefully controlling both the Capillary number and the degree of confinement through adjustments in flow rates and channel geometry, it is possible to finely tune droplet size, shape, and formation frequency. This control enables the optimization of droplets for microreactor applications. While the main droplet generation region was maintained consistently across the studied geometries, subsequent modifications to channel length and shape provided additional means to regulate mixing characteristics and confinement effects.

B. Computational fluid dynamics simulations

A novel Computational Fluid Dynamics (CFD)-based multi-modal optimization methodology is introduced to explore the influence of geometry, flow parameters, and initial concentrations on the evolving concentration distribution in a multi-phase microfluidic system. This study investigates the impact of geometry and flow parameters on mixing phenomena in forming microdroplets, including Dean vortices and resulted mixing efficiency[15,16]. The Finite Element Method (FEM) based COMSOL Multiphysics software is utilized to simulate the droplet formation process as in[17]. In comparison, this study is a three-dimensional (3D) three-phase model[18], providing a precise understanding of flow characteristics and their influence on concentration transfer mechanisms. Water and aqueous solution of fluorescently labeled BSA were injected parallel as the dispersed phase, forming quasi-monodisperse droplets in a silicon oil-based continuous phase. The investigation is based on the numerical solution of the Navier–Stokes and continuity equations[19]:

$$\rho\left(\frac{\partial u}{\partial t}+u\cdot\nabla u\right)=-\nabla p+\nabla\cdot\left(\mu\left(\nabla u+(\nabla u)^{T}\right)-\frac{2}{3}\mu\left(\nabla\cdot u\right)I\right)+F \tag{2}$$

$$\frac{\partial\rho}{\partial t}+\nabla\cdot(\rho u)=0 \tag{3}$$

Equation (2), the Navier–Stokes equation, is a set of partial differential equations that describe fluid motion by relating the flow velocity (or momentum) and pressure. The left-hand side represents the product of density and total acceleration (local and convective) of the fluid. The right-hand side represents the sum of forces per unit volume acting on an infinitesimal fluid element. Here, ρ is the density, u is the flow velocity vector, p is the pressure, μ is the dynamic viscosity, and F represents external body forces, such as gravity or thermal fluctuations. Equation (3) is the continuity equation enforcing mass conservation.

For the ternary fluid model, the effective viscosity and density of the fluid mixture are expressed as weighted sums of the individual phase properties based on the phase field variables ϕ_i[19]:

$$\mu=\mu_A\phi_A+\mu_B\phi_B+\mu_C\phi_C, \tag{4}$$

$$\rho=\rho_A\phi_A+\rho_B\phi_B+\rho_C\phi_C, \tag{5}$$

where ϕ_i denote the volume fractions of the three immiscible phases A, B, and C.

In the droplet generation process, the influence of the volume flow ratio of the different phases at the inlets was studied through systematic parametric sweep simulations. To capture the interfaces between the immiscible fluids (oil, water, and fluorescent solution), the ternary phase field method was employed, considering surface tension and contact angle effects. This approach shares conceptual similarities with Level Set and two-phase Phase Field models[20]. A key parameter in the phase field model is the interface thickness ϵ, which controls the resolution of the diffuse interface. The interface thickness was set to the default value computed based on the mesh size and relevant physical scales, providing a balance between numerical stability and physical accuracy.

The body force term F in Eq. (2) includes capillary forces arising from interfacial tension, which are derived from the ternary phase field model and computed as

$$F_{\mathrm{st}}=\sum_{i=A,B,C}\eta_i\nabla\phi_i, \tag{6}$$

where η_i are the chemical potentials associated with the phase field variables ϕ_i. This surface tension force is incorporated as a volumetric body force in the Navier–Stokes equation within COMSOL Multiphysics, enabling seamless coupling between fluid mechanics and interface dynamics. Other external forces, such as grav-

ity, magnetic fields, and thermal fluctuations, are neglected due to their negligible influence at the microscale.

Another crucial parameter in the phase field model is the mobility tuning parameter (M_0), which facilitates accurate interface tracking. In this study, M_0 was set to $1{\cdot}10^{-10}$ m^3/s, based on a balance between physical accuracy and numerical stability under the given microfluidic conditions. Due to the low Reynolds number and low flow rates in the system, inertial effects are negligible, allowing the mobility parameter to predominantly govern the interface dynamics.

The model employs a free energy formulation with three-phase field variables corresponding to phases A, B, and C. The phase boundary is defined by an isosurface of a phase field variable at 0.5, ensuring that at each point, the sum of the phase field variables equals 1, representing the composition of each phase. These variables and the surface tensions of each boundary interface influence the system's free energy, governed by the Cahn-Hilliard equation[19].

$$\frac{\partial \phi_i}{\partial t} = M\nabla^2 \left(\frac{\delta \Psi}{\delta \phi_i} - \sum_{j \neq i} \gamma_{ji} \nabla^2 \phi_j \right) \tag{7}$$

where: ϕ_i is the phase field variable for phase i, M is the mobility coefficient, Ψ is the free energy functional, γ_{ji} is the surface tension coefficient between phase j and i, and ∇^2 represents the Laplacian operator. To model three-phase flows, the Cahn-Hilliard equations (7) are then coupled with the Navier-Stokes equations (2).

The free energy functional Ψ is defined as:

$$\Psi = \int_\Omega \left[\sum_{i=1}^{3} \left(\frac{\epsilon^2}{2} |\nabla \phi_i|^2 + \frac{W}{4} \phi_i^2 (1 - \phi_i)^2 \right) + \kappa \phi_1 \phi_2 \phi_3 \right] d\Omega \tag{8}$$

where ϕ_i are the phase field variables for phases A, B, and C; ϵ is the gradient energy coefficient controlling interface thickness; W defines the depth of the double-well potential, which stabilizes pure phases by favoring phase field values close to 0 or 1; and κ is a coupling coefficient that governs the interaction between the three phases at triple junctions, influencing the morphology and dynamics of the system during phase separation and mixing. The free energy functional Ψ accounts for both bulk free energy and interfacial contributions, determining the evolution of the phase field variables via the Cahn–Hilliard equations. The gradient energy term penalizes sharp changes in the phase fields, thereby controlling the thickness and energy of the interfaces. The bulk free energy density $\mathcal{F}(\boldsymbol{\phi})$ governs the thermodynamic preference for each pure phase and penalizes mixed states, defined as:

$$\mathcal{F}(\boldsymbol{\phi}) = \sum_{(i,j)} \sigma_{ij} \phi_i^2 \phi_j^2 + \sum_{(i,j,k)} \sigma_{ij} \phi_i^2 \phi_j \phi_k, \tag{9}$$

where the first summation runs over all unique pairs of phases i, j in A, B, C, and the second summation extends over all unique triples i, j, k of distinct phases. The variables ϕ_i denote the phase field parameters corresponding to phases $i = A, B, C$, and σ_{ij} represent the interfacial tension coefficients between phases i and j. This formulation energetically penalizes mixed or intermediate states, thereby stabilizing pure phases by minimizing the free energy in such configurations and promoting phase separation.

The interaction with the walls is determined by the fixed contact angles (θ_i). The contact angles define boundary conditions for each phase field variable at the walls, ensuring a hydrophobic surface to prevent droplet sticking. The contact angle was adjusted to be 90°. Surface tension forces are incorporated into the Navier-Stokes equations as momentum sources, with each phase characterized by its density and viscosity, transitioning smoothly at a phase field value of 0.5.

The Transport of Diluted Species[21] model was used alongside the Ternary Phase Field method and the Laminar Flow module to calculate concentration distribution in microdroplets. This setup analyzes transport and reactions in dissolved phases, considering mechanisms like diffusion (Fick's law), convection, and migration. The model tracks molar concentrations (c_i) of each phase, such as water, silicon oil, and BSA in our case. The transport equation is[22]:

$$\frac{\partial(\theta C_i)}{\partial t} = \nabla \cdot (D_{\text{eff},i} \nabla C_i) - \nu \cdot \nabla C_i + R_i \tag{10}$$

whereθ_i represents the saturation level, v denotes the convective velocity, and C_i is the concentration of the i-th substance or phase. $D_{eff,i}$ refers to the effective diffusivity of the i-th phase, while R_i signifies the reaction rate for each respective phase. Notably, R_i was set to zero across all phases and models for this analysis. When fluid motion is involved, the module integrates phase transport modeling with fluid flow by employing a convective transport mechanism to capture these dynamics.

C. Materials and transport parameters

COMSOL Multiphysics software includes built-in material libraries. For this study, the main material properties are shown in Table II. Accordingly, the built-in attributes of distilled water were used for the material properties from the Material Library. However, in the case of the silicon oil the density has been set to ρ=1000 kg/m^3, and the dynamic viscosity was defined as μ=0.02 Pa·s based on the properties of the silicon oil (Sigma Aldrich – CAS 63148-58-3)[23], which has been used in the laboratory. In terms of the BSA solution, the parameters were ρ=1030 kg/m^3 and μ=0.001 Pa·s, as we found in the literature search[24]. The transport properties are detailed in Table III, based on literature and laboratory measurements. The simulation used a "finer" mesh with element sizes ranging from 13 μm to 1.5 μm, totaling 113,832 elements. The mesh element size was calibrated for fluid dynamics with a triangular meshing grid method. Regular refinement was also applied to the droplet-forming domain. The time-dependent CFD simulation ran from 0 to 0.08 s with a time step of $2 \cdot 10^{-5}$s.

TABLE II. Main Parameters of Materials.

Material	Dynamic Viscosity (μ)	Density (ρ)
Distilled Water	$0.89 \cdot 10^{-3}$ Pa·s	10^3 kg/m^3
Silicon Oil	$20 \cdot 10^{-3}$ Pa·s	10^3 kg/m^3
BSA Solution	10^{-3} Pa·s	$1.03 \cdot 10^3$ kg/m^3

TABLE III. Main Transport Properties.

Material	Concentration (C_i)	Diffusion coefficient (D_{ci})
Distilled Water	55 mol/m^3	$2.3 \cdot 10^{-9}$ m^2/s
Silicon Oil	10 mol/m^3	$0.5 \cdot 10^{-10}$ m^2/s
BSA Solution	$1.51 \cdot 10^{-4}$ mol/m^3	$6.7 \cdot 10^{-11}$ m^2/s

III. RESULTS AND DISCUSSION

A. Non-mixing phenomenon at low flow rates

To establish conditions for three-phase flow within the microfluidic channel, appropriate material properties were assigned to represent the behavior of the involved phases accurately. The inlet boundaries were defined with specific volumetric flow rates for each liquid phase, while the outlet boundary was set to a zero-pressure condition to facilitate unimpeded flow. Additionally, the fluid properties were configured under the 'incompressible fluid' assumption, ensuring consistent simulation of the fluid dynamics. The initial flow rates were specified as 0.2 μl/s for water, 0.2 μl/s for the BSA solution, and 0.02 μl/s for oil. These flow conditions resulted in a visualization of the three-phase distribution, which revealed minimal mixing between the phases, as depicted in Fig. 2.

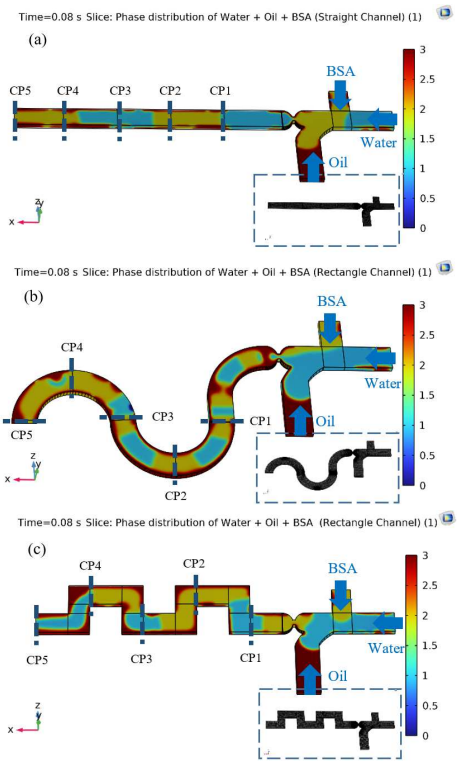

FIG. 2. Continuous flow in the three different 3D microfluidic channels: (a) straight channel, (b) curved channel, and (c) rectangular channel. The different fluids—oil, water, and BSA solution—are represented by the colors red, blue, and yellow, respectively. It can be clearly seen that no special mixing processes take place in the channel, the phases flow one after the other. The non-mixing phenomenon has also been analyzed in laboratory experiments.

The simulation also highlighted the transient nature of the phase distribution within the channel, where variations in the combined effect of the three-phase field variables became apparent. Specifically, regions with higher phase values (indicated by yellow/red) were distinguishable from regions with lower phase values (indicated by blue). Cutplanes (CP1-5) were placed on certain segments of the channels, which played an important role in the subsequent calculations.

B. Mixing phenomenon and concentration profile in microdroplets

To investigate the effects of droplet formation on phase transport, the flow rates were modified to achieve the droplet generation regime. The adjusted rates were set to 0.2 μl/s for water, 0.2 μl/s for the BSA solution, and 1.4 μl/s for the oil phase. This adjustment created a flow rate ratio of 3.5:1 between the continuous (oil) and dispersed (water and BSA) phases, ensuring the conditions necessary for consistent droplet formation, as illustrated in Fig. 3.

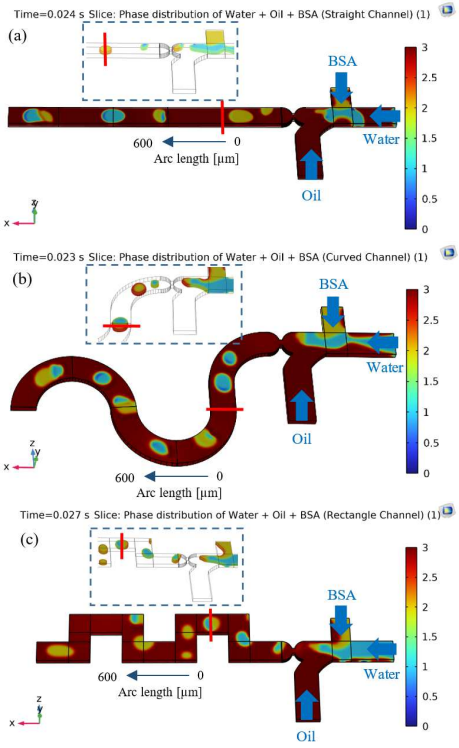

FIG. 3. Droplet generation in the 3D channels. To determine the droplet diameter, a boundary probe was set in the middle of the channel (marked with a red line), and an integrator operator was used along the probe for calculations. The average diameter was 184.1 μm in the straight channel (a), 186.7 μm in the curved geometry (b), and 188.6 μm in the rectangle structure (c).

Contour lines were applied at the interface where the three fluids meet, capturing the behavior of the system at this critical juncture. These interfaces were dynamically displaced, primarily driven by high-pressure fluctuations occurring at narrower cross-sections of the channel. This interplay of forces led to the segmentation of the dispersed phase into discrete droplets. Additionally, for the 3D plot, a slice plot option was incorporated with a color expression, regulated to the volume fraction of the fluids.

In Fig. 4, the 1D plot of cut lines illustrates the variation in concentration as a function of the distance from the channel inlet.

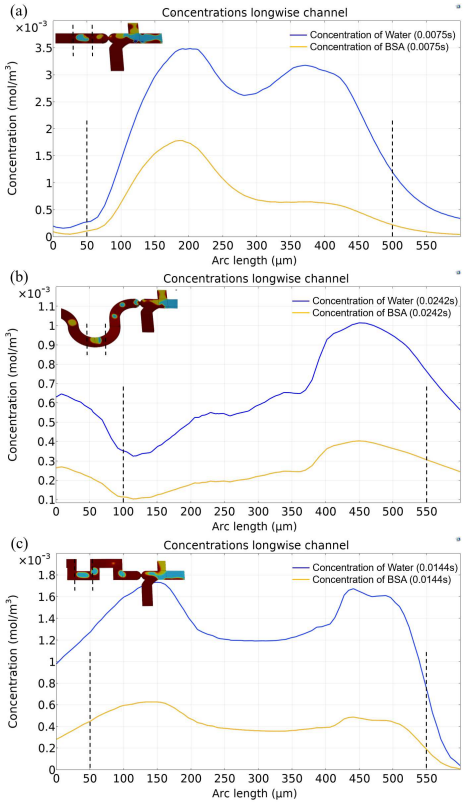

FIG. 4. Concentration changes along the channel in the case of straight (a), curved (b), and rectangle (c) channel types. The change in concentration is visible when the droplets pass through the examined section, which shows that there is no significant diffusion of the liquids through the wall of the droplet. This enclosed environment enables droplets to function as isolated microreactors for mixing.

This analysis highlights how the concentration evolves along the flow direction within the three-phase microfluidic system. The periodic nature of the concentration distribution is particularly evident, reflecting the repetitive formation of droplets and their associated boundary effects within the flow regime. The plot demonstrates

that the concentration of the mixed water and BSA solution experiences a marked reduction as it crosses the boundary surface of individual droplets. This reduction is indicative of the transport and mixing processes occurring within the system, where the boundary layer at the droplet interface plays a critical role in regulating the exchange of material between the phases. The periodic behavior observed in the concentration profile provides insight into the interaction dynamics within the droplets and their surroundings.

Additionally, the concentration distribution of water and BSA within the droplets becomes increasingly uniform as the droplets travel through the microfluidic channel, eventually achieving a higher degree of homogeneity by the time they reach the channel's outlet. This observation, depicted in Fig. 5, indicates that the mixing processes within the droplets are effectively facilitated by the flow dynamics and the specific channel geometry throughout their movement. Factors such as the curvature of the channel, droplet deformation, and the interplay of shear forces likely contribute to this enhanced mixing.

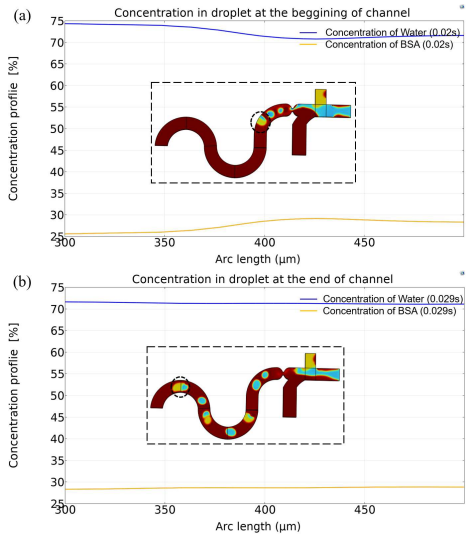

FIG. 5. Relative concentration distribution of water and BSA in the droplet when it is at the beginning of the channel (a) and then at the end of the channel (b) in case of the curved type geometry.

In curved microfluidic channels, laminar Poiseuille flow is influenced by centrifugal forces generated due to the channel's curvature. These forces cause the fluid velocity profile to shift—the maximum velocity moves from the centerline toward the concave (inner) wall of the channel. This shift creates a steeper velocity gradient and increases pressure differences across the channel cross-section. The resulting imbalance near the walls leads to the formation of Dean vortices: pairs of counter-rotating secondary vortices that arise perpendicular to the main flow direction[25]. These vortices result from the interplay between the centrifugal forces pushing the fluid outward and the viscous forces resisting this motion. They play a critical role in enhancing mixing and mass transport in curved microchannels. The strength and presence of these vortices are characterized by the Dean number (De), a dimensionless parameter that quantifies the ratio of inertial to viscous forces in curved channels. Fig. 6 shows the development of these vortices at a specific vertical flow rate in the curved section of the second channel geometry.

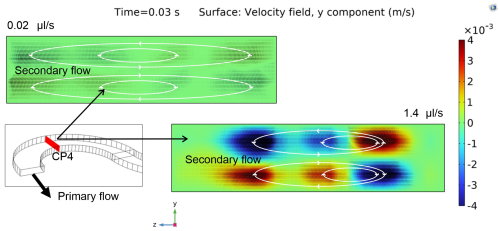

FIG. 6. Dean vortices were observed in the curved section of the second channel geometry. A cut plane (CP4) was placed at the midpoint of the second curve within the 3D channel to analyze the flow dynamics.

To evaluate the Dean vortices, a cut plane was added to the simulation. Here, the y-component of the velocity field in the microfluidic channel was investigated at different regions of the curved section. On the fourth cut plane, velocity components orthogonal to the primary flow direction was examined to capture the characteristic swirling motion induced by curvature. The vortices began to appear at even lower flow rates, although the secondary velocity components intensified when the oil flow was accelerated from 0.02 μl/s to 1.4 μl/s. Fig. 6 demonstrates the flow rate dependent shift of the center of the vortex towards the outer wall of the bend.

The mixing efficiency (ME) was evaluated using the following equation:

$$ME = \left(1 - \frac{\sqrt{\sigma^2}}{\sqrt{\sigma_0^2}}\right) \times 100\% \tag{11}$$

where σ_0^2 represents the concentration variance at the start of the mixing channel, where the fluid is in an unmixed state, meanwhile, σ^2 denotes the concentration variance at a specific cross-section along the channel. The results of the investigation of mixing efficiency (11) are illustrated in Fig. 7.

The results demonstrate that the curved channels, represented in red, exhibited the highest mixing efficiency

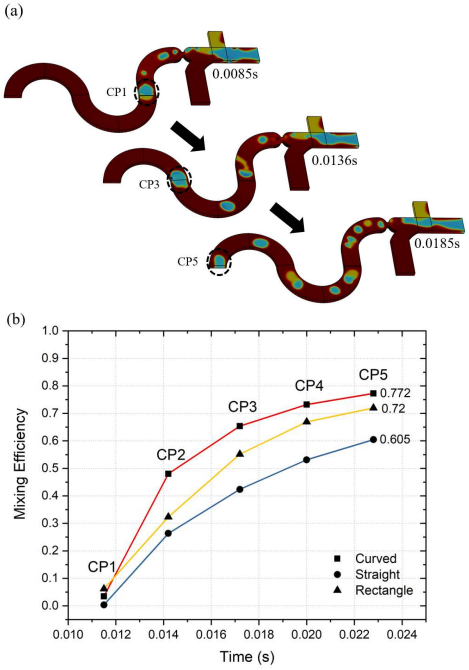

FIG. 7. Droplets pass through cut-planes positioned along the curved channel (a). Mixing efficiency across five cut-planes for the three channel geometries as the droplets advance along the flow path (b).

at 0.772, outperforming the straight channels, depicted in blue, and the rectangular channels, shown in yellow, which achieved mixing efficiencies of 0.605 and 0.72, respectively. This finding supports the capability of curved channels to facilitate more effective mixing. This advantage is likely attributed to the generation of secondary flow structures, such as Dean vortices, which promote enhanced mixing by intensifying fluid interaction across various layers, thereby achieving a more thorough blending of the substances.

IV. MESH CONVERGENCE STUDY

A convergence study was conducted to see how mixing efficiency is affected by mesh resolution. The parameters of the different meshes are shown in Table IV.

The lowest and highest mesh resolutions and droplet formation process can be seen in Fig. 8.

In the coarser mesh, larger elements reduce the resolution of fluid dynamics, leading to a less accurate representation of the droplet interface and breakup processes.

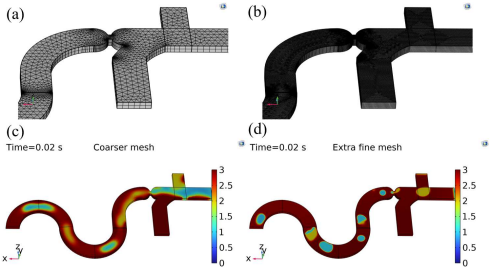

FIG. 8. Illustration of the coarser mesh (a) and extra fine mesh (b) configurations utilized in the convergence study, showcasing the significant impact that varying mesh resolutions have on the dynamics of droplet formation (c, d).

This can result in irregular droplet shapes and underestimated forces. In contrast, the extra fine mesh, with smaller elements, provides higher resolution, accurately capturing droplet deformation, breakup, and interactions like shear and interfacial tension, yielding results closer to physical behavior.

The relationship between mixing efficiency and mesh resolution was thoroughly examined and is shown in Fig. 9. The mesh convergence study indicates that the mixing efficiency stabilizes between 0.76 and 0.77 as the mesh resolution increases. This suggests that the simulation has achieved mesh independence, where further mesh refinement no longer significantly affects the results. A clear trend is observed: the mixing efficiency at the channel outlet (CP5) progressively improves with increasing mesh resolution. This improvement continues up to a certain threshold mesh configuration, beyond which additional refinement does not yield any noticeable enhancement in mixing efficiency, indicating convergence in the results.

V. EXPERIMENTAL VALIDATIONS

Experimental measurements were also conducted to support the simulations (Fig. 10). The experimental work was carried out in the Microsystems Laboratory of the HUN-REN Centre for Energy Research, where basic microtechnological and micromechanical steps were utilized for processing microfluidic systems.

Soft lithography, recognized as one of the most efficient techniques for processing microfluidic structures, was utilized to fabricate the structures in PDMS (polydimethylsiloxane) polymer material through a casting method. A custom-designed mechanical syringe pump was employed to introduce the liquids into the system. The operation of the implemented microfluidic chips was examined using darkfield and fluorescence microscopy. During the measurements, the Zeiss Axio Vert A1 inverted microscope was applied.

TABLE IV. Main Properties of Different Meshes Applied.

Type	Maximum element size (μm) (C_i)	Minimum element size (μm)	Number of elements
Coarser	42.4	13	9530
Coarse	32.6	9.78	14744
Normal	21.8	6.52	38469
Fine	13	1.5	113832
Finer	12.1	1.3	152820
Extra Fine	7.5	0.49	428449

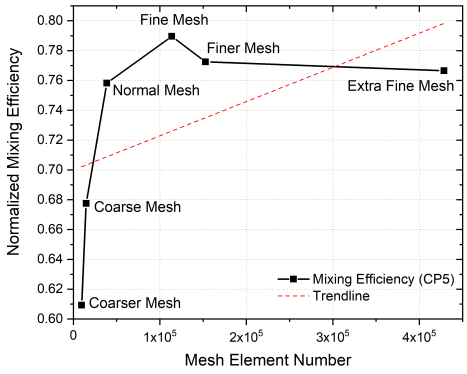

FIG. 9. The change of the mixing efficiency at the outlet of the channel (CP5) in case of different mesh resolutions.

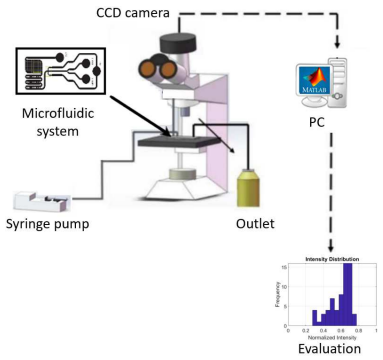

FIG. 10. Measurement setup for the experimental validations.

The calibration of flowrates to generate microdroplets is shown in Fig. 11. The adjusted flowrates were set to 0.1 μl/s for water, 0.1 μl/s for the BSA solution, and 0.1 μl/s for the oil phase in the first case to see the three liquid flows separated in the microfluidic channels. Then, the flow rate was changed to 0.2 μl/s for water, 0.2 μl/s for the BSA solution, and 0.5 μl/s for the oil phase to generate microdroplets.

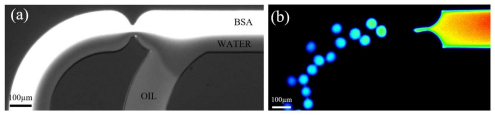

FIG. 11. The picture from the experimental studies represents the continuous flow (a) and droplet formation (b) during the laboratory measurements.

After setting the proper flow rates, the regime of droplet formation was achieved, showing vortices inside the droplet at the moment of detachment (Fig. 12). The appearance of turbulent force in this stage is not sufficient to create efficient mixing.

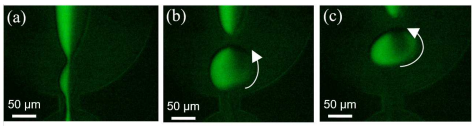

FIG. 12. Initial vortex formation during droplet detachment. Droplet elongation prior to detachment (a). Vortex appears inside the droplet at the moment of detachment (b). Vortex development continues inside the fully detached droplet (c).

To see more significant mixing inside the droplets the flow rates were changed to generate droplets with size comparable to the channel width (Fig. 13.a,b).

When the droplets reach the first section of the serpentine channel, the oil rind surrounding the droplets undergoes torsional effects, causing the droplets to deform, which significantly promotes mixing. Due to this and the centrifugal forces acting in the bends, Dean vortices can be seen within the droplets. To provide additional evidence for this phenomenon, fluorescent microbeads were introduced into the droplets, allowing for a clearer visualization of how the generated vortices influence the movement and behavior of the beads within the droplets (Fig. 13.c,d).

Finally, the concentration distribution and concentration profile of BSA in the droplets were investigated, creating a population of droplets with different concentrations. The results can be seen in Fig. 14. For

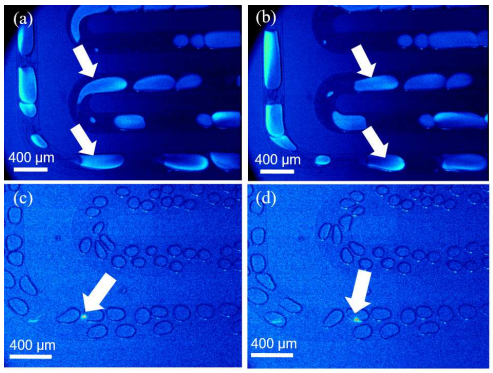

FIG. 13. Investigating the Dean vortices inside droplets (a,b). The microbeads perform a rotational motion inside the droplets at the winding channels due to the centrifugal force (c,d).

the analysis, MATLAB software was utilized extensively. The script demonstrated the capability to identify the droplets present in the exported images and to calculate their individual and average diameters, which, in this case, was determined to be 60.56 μm. To explore the distribution of BSA concentration within the droplets, a pure BSA solution was used as a reference (Fig. 11.a). Once the droplets were detected, the MATLAB script proceeded to calculate the fluorescent intensity of each droplet within the exported images. This intensity is directly proportional to the concentration of BSA within the droplets, making it a reliable indicator of protein distribution. By quantifying the intensity, it was possible to infer variations in BSA concentration across the droplets, providing valuable insights into the flow control and fluctuation, or the mixing efficiency by analyzing intensity homogeneity. Additionally, the intensity profile of ten randomly selected droplets was analyzed using ImageJ. In this step, the intensity variation was determined along a line drawn through the center of each selected droplet, providing further insight into the spatial distribution of BSA within the droplets.

As a practical application of the experimental results, an illustrative example is provided, where a larger population of droplets is analyzed. In this scenario, droplets with higher BSA concentrations were specifically selected. Based on the previous approach, the MATLAB script detected the population, and the normalized intensity was calculated for each droplet to be classified and labeled as presented in Fig. 15. The intensity and size distribution of the droplet population was also determined as shown in Fig. 16.

This approach demonstrates a potential pathway for future applications, where BSA can be substituted with a fluorescent therapeutic drug such as doxorubicin[26–28].

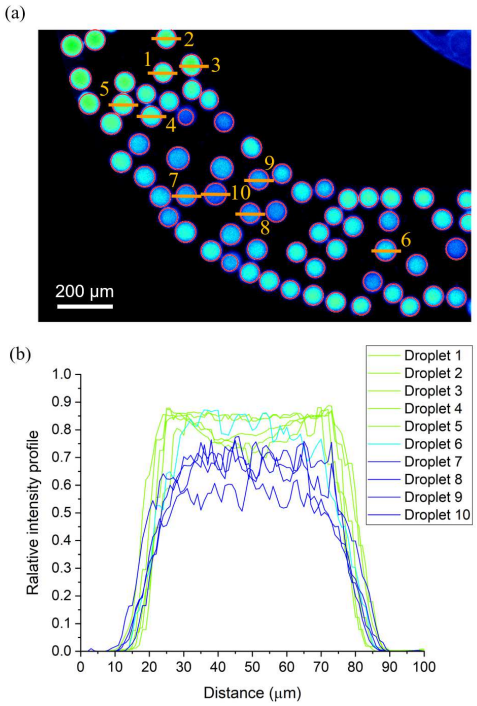

FIG. 14. Detection of microdroplets in microfluidic channels by image processing (a). ImageJ and MATLAB software were used to calculate the intensity profiles (b) of the microdroplets.

Doxorubicin is a widely studied chemotherapeutic agent that plays a pivotal role in cancer research due to its effectiveness in inhibiting the proliferation of cancer cells. Precise dosing is critical, as insufficient concentrations may fail to eliminate the cancer cells, while excessive dosages can lead to severe side effects. The intensity of the droplets in the experimental setup directly correlates with the concentration of BSA and, by extension, could be used to infer the concentration of doxorubicin when used as a replacement. This relationship highlights the potential for using the intensity profiles of droplets to identify those containing the optimal drug concentration. Such a methodology could aid in selecting appropriately dosed droplets for targeted cancer therapy, utilizing the droplets as microreactors to treat cancer cell populations effectively while minimizing the risk of adverse effects.

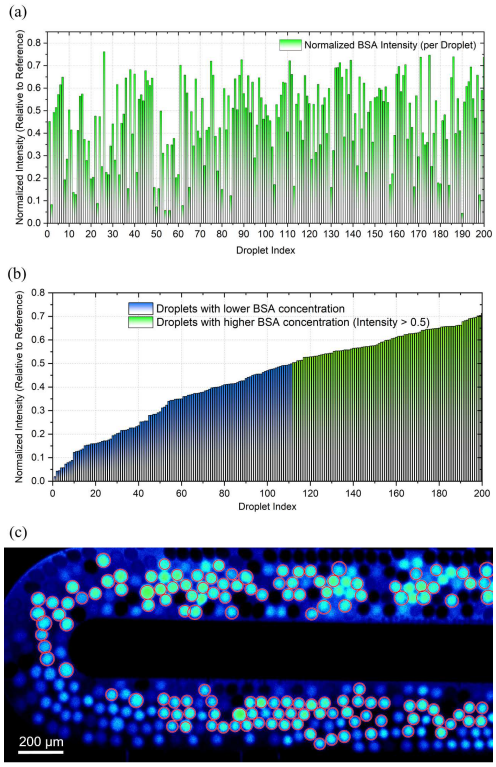

FIG. 15. Normalized fluorescent intensities characterize the individual droplets in the population (a). The intensities were plotted in order of increasing concentration, from the lowest to the highest (b). In this plot, droplets with an intensity greater than 0.5 were marked in green. These selected droplets are also highlighted in image (c), demonstrating an approach to detect droplets with higher concentrations of BSA easily.

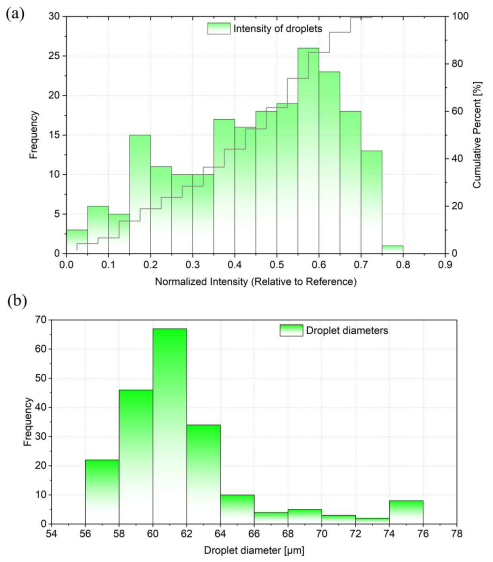

FIG. 16. The number of droplets with a given BSA concentration related fluorescent intensity (a) and diameter (b) in the population of 200 droplets, with an average diameter of 62.48 μm.

VI. CONCLUSION

The comprehensive investigation of mixing phenomena within microdroplets in a simulation environment is essential for understanding the underlying physical processes and predicting the behavior of complex microfluidic systems. Finite Element Modeling enables the analysis of parallel processes, such as droplet formation and mixing, through 3D multi-phase models, facilitating the estimation of concentration distribution within these microfluidic environments. Among the configurations explored, the serpentine channel proved to be the most effective, achieving the highest mixing efficiency and promoting a more uniform chemical microenvironment. This performance is attributed to the generation of Dean vortices and enhanced internal circulation, which improve the homogenization of solutes like therapeutic agents. Complementary experimental studies supported these findings, underscoring the reliability of the computational predictions and emphasizing the importance of precise design in microfluidic systems. While previous studies have thoroughly examined passive and active mixers, Dean vortices, droplet-based mixing, and numerical modeling techniques, this research advances the field by utilizing a 3D, three-phase model to study microdroplet mixing with a specific focus on pharmaceutical applications. This novel approach offers a more accurate representation of the behavior of active compounds compared to the primarily two-phase models used in earlier works. Future research could expand on these findings by exploring additional therapeutic agents and channel geometries, further enhancing the versatility and applicability of these systems for controlled chemical environments, such as single-cell studies, drug delivery, and droplet biochemical reactions.

ACKNOWLEDGMENTS

Funding for the study was provided by the Ministry of Innovation and Technology of Hungary from the National Research, Development and Innovation Fund (NK-

FIA) via INBIOM TKP2021-EGA-04 grant. The authors would also like to thank the Estonian Research Council for the support provided under projects PRG620 and PSG897. The kind support of TalTech ERASMUS+ programme is gratefully acknowledged (recipient: Nafisat Gymah).

This article is a revised and extended version of a paper entitled 3D Finite Element Modelling of Mixing Phenomena in Droplet-based Microfluidic Systems, which was presented at the 19^{th} Biennial Baltic Electronics Conference (BEC), Tallinn, Estonia, 2–4 October 2024[29].

DATA AVAILABILITY

The data that support the findings of this study are available from the corresponding author upon reasonable request.

[1] H. Zhu, Z. Fohlerová, J. Pekárek, E. Basova, and P. Neuzil, "Recent advances in lab-on-a-chip technologies for viral diagnosis," Biosensors and Bioelectronics **153** (2020), 10.1016/j.bios.2020.112041.
[2] O. Scheler, K. Makuch, P. R. Debski, M. Horka, A. Ruszczak, N. Pacocha, K. Sozanski, O. P. Smolander, W. Postek, and P. Garstecki, "Droplet-based digital antibiotic susceptibility screen reveals single-cell clonal heteroresistance in an isogenic bacterial population," Scientific Reports **10**, 3282 (2020).
[3] D. Liu, M. Sun, J. Zhang, R. Hu, W. Fu, T. Xuanyuan, and W. Liu, "Single-cell droplet microfluidics for biomedical applications," Analyst **147**, 2294–2316 (2022).
[4] X. Chen, T. Li, and Z. Hu, "A novel research on serpentine microchannels of passive micromixers," Springer-Verlag, Berlin (2016), 10.1007/s00542-016-3060-7.
[5] C. Chen, Y. Zhao, J. Wang, P. Zhu, Y. Tian, M. Xu, L. Wang, and X. Huang, "Passive mixing inside microdroplets review," Micromachines **9**, 160 (2018).
[6] L. Yan, S. Li, J. Liu, and J. Cheng, "Fluid mixing in droplet-based microfluidics with t junction and convergent-divergent sinusoidal microchannels," Electrophoresis **39**, 512–520 (2018).
[7] M. Paz and W. Leigh, "Introduction to finite element method," in *Integrated Matrix Analysis of Structures* (Springer US, 2001) pp. 261–300.
[8] "Sigma-aldrich product information sheet - b4287," (), accessed: 2024-07-25.
[9] C. Wei, C. Yu, S. Li, F. Pan, T. Li, Z. Wang, and J. Li, "Rapid microfluidic mixing method based on droplet rotation due to PDMS deformation," Micromachines (2001).
[10] A. Pishkoo and M. Darus, "Using fractal calculus to solve fractal navier–stokes equations, and simulation of laminar static mixing in COMSOL multiphysics," (2021).
[11] P. Poureslami, M. Majidi, J. R. Kermani, and M. A. Bijarchi, "Deformation and breakup of a ferrofluid compound droplet migrating in a microchannel under a magnetic field: A phase-field-based multiple-relaxation time lattice Boltzmann study," Physics (2025), 10.48550/arXiv.2410.11129.
[12] W. Lee, L. M. Walker, and S. L. Anna, "Role of geometry and fluid properties in droplet and thread formation processes in planar flow focusing," Physics of Fluids **21** (2009), 10.1063/1.3081407.
[13] H. Gu, M. H. G. Duits, and F. Mugele, "Droplets formation and merging in two-phase flow microfluidics," International Journal of Molecular Sciences (2011), 10.3390/ijms12042572.
[14] K. He, Z. Zhang, L. Zhang, and W. Yuan, "Effects of geometrical confinement on the generation of droplets at microfluidics t-junctions with rectangle channels," Microfluidics and Nanofluidics (2023), 10.1007/s10404-023-02678-9.
[15] P. B. H. Jr, D. R. Mott, J. P. Golden, and F. S. Ligler, "Design and evaluation of a dean vortex based micromixer," Lab. Chip **4**, 663–669 (2004).
[16] I. A. Dagga and M. Abdelgawad, "Numerical modeling of sequential segmentation for enhancement of mixing inside microchannels," International Journal of Thermofluids (2022), 10.1016/j.ijft.2022.100207.
[17] K. Pärnamets, A. Udal, A. Koel, T. Pardy, N. Gyimah, and T. Rang, "Compact empirical model for droplet generation in a lab-on-chip cytometry system," IEEE Access **10**, 127708–127717 (2022).
[18] "Simulate three-phase flow with a new phase field interface," https://www.comsol.com/blogs/simulate-three-phase-flow-with-a-new-phase-field-interface/, accessed: 2024-05-13.
[19] A. O. Jegede, C. Gualtieri, G. Zeeman, and H. Bruning, "Three-phase simulation of the hydraulic characteristics of an optimized chinese dome digester using COMSOL multiphysics," Renewable Energy **157**, 530–544 (2020).
[20] "Two methods for modeling free surfaces in COMSOL multiphysics," https://www.comsol.com/blogs/two-methods-for-modeling-free-surfaces-in-comsol-multiphysics, accessed: 2024-05-13.
[21] "COMSOL documentation: Chemical species transport," Accessed: 2024-05-13.
[22] E. L. Cussler, *Diffusion: Mass Transfer in Fluid Systems* (Cambridge University Press, 2009).
[23] "Sigma-aldrich product information - aldrich/10836," (), accessed: 2024-05-13.
[24] "VROC initium application note: BSA formulations," https://www.cas-instrumental.com.ar/wp-content/uploads/2019/02/VROC-initium-APP01-4-16-BSA-Formulations-Final.pdf, accessed: 2024-05-13.
[25] A. Bányai, E. L. Tóth, M. Varga, and P. Fürjes, "Geometry-dependent efficiency of dean-flow affected lateral particle focusing and separation in periodically inhomogeneous microfluidic channels," Sensors **22**, 3474 (2022).
[26] O. Tacar, P. Sriamornsak, and C. R. Dass, "Doxorubicin: an update on anticancer molecular action, toxicity and novel drug delivery systems," Journal of Pharmacy and Pharmacology **65**, 157–170 (2013).
[27] S. hsuan Wen, S. chiang Su, B. huang Liou, C. hao Lin, and K. rong Lee, "Sulbactam-enhanced cytotoxicity of doxorubicin in breast cancer cells," Cancer Cell International **18**, 128 (2018).
[28] J. Lee, M.-K. Choi, and I.-S. Song, "Recent advances in doxorubicin formulation to enhance pharmacokinetics and tumor targeting," Pharmaceuticals **16**, 802 (2023).
[29] Z. Szomor, N. Gyimah, T. Pardy, and P. Fürjes, "3D finite element modelling of mixing phenomena in droplet-based microfluidic systems," 19th Biennial Baltic Electronics Conference (BEC) (2024), 10.1109/BEC61458.2024.10737975.